Conformational change in the monomeric alpha-synuclein imparts fibril polymorphs

Cesar Aguirre[1,†], Kensuke Ikenaka[1*,†], Masatomo So[2], Takahiro Maruno[3], Keiichi Yamaguchi[4], Kichitaro Nakajima[4], Chi-Jing Choong[1], Kei Nabekura[1], Goichi Beck[1], Kentaro Tomii[5], Yu Yamamori[5], Junko Doi[1], Tomoyasu Matsubara[6], Maho Morishima[6], Keita Kakuda[1], Makoto Hideshima[1], Nan Wang[1], Takahiro Ajiki[1], Shaymaa Mohamed Mohamed Badawy[1,7], Yasuyoshi Kimura[1], Seiichi Nagano[1], Kousuke Baba[1], Shigeo Murayama[6,8], Hirotsugu Ogi[4], Yoshitaka Nagai[9], Yasushi Kawata[10], Susumu Uchiyama[3], Yohei Miyanoiri[11], Yuji Goto[4], and Hideki Mochizuki[1*]

[1] Department of Neurology, Osaka University Graduate School of Medicine, 2-2 Yamadaoka, Suita, Osaka 565-0871, Japan.

[2] Institute for Protein Research, Osaka University, Japan, 3-2 Yamadaoka, Suita, Osaka 565-0871, Japan.

[3] Department of Biotechnology, Graduate School of Engineering, Osaka University, Japan, 2-1 Yamadaoka, Suita, Osaka 565-0871, Japan.

[4] Graduate School of Engineering, Osaka University, Japan, 2-1 Yamadaoka, Suita, Osaka 565-0871, Japan.

[5] Artificial Intelligence Research Center (AIRC), National Institute of Advanced Industrial Science and Technology (AIST), 2-4-7 Aomi, Koto-ku, Tokyo, 135-0064, Japan.

[6] Department of Neuropathology (the Brain Bank for Aging Research), Tokyo Metropolitan Geriatric Hospital and Institute of Gerontology, 35-2 Sakae-cho, Itabashi-ku, Tokyo, 173-0015, Japan.

[7] Department of Agricultural Biochemistry, Faculty of Agriculture, Zagazig University, Zagazig, Egypt.

[8] Brain Bank for Neurodevelopmental, Neurological and Psychiatric Disorders, United Graduate School of Child Development, Osaka University, 2-2, Yamadaoka, Suita- shi, Osaka, 565-0871, Japan.

[9] Department of Neurology, Faculty of Medicine, Kindai University, Osaka-Sayama, Osaka, Japan.

[10] Department of Chemistry and Biotechnology, Graduate School of Engineering, Tottori University, Tottori 680-8552, Japan.

[11] Laboratory for Ultra-High magnetic field NMR spectroscopy, Research Center for Next-Generation Protein Sciences, Institute for Protein Research, Osaka University, Japan, 3-2 Yamadaoka, Suita, Osaka 565-0871, Japan.

*Correspondence to Dr. Kensuke Ikenaka, M.D, Ph.D., and Prof. Hideki Mochizuki, M.D., Ph.D.

Department of Neurology, Osaka University Graduate School of Medicine, 2-2 Yamadaoka, Osaka 565-0871, Japan. Phone: 81-6-6879-3571.

E-mail: ikenaka@neurol.med.osaka-u.ac.jp, hmochizuki@neurol.med.osaka-u.ac.jp

† These authors contributed equally to this work.

Manuscript has been deposited as preprint in Biorxkiv:

https://www.biorxiv.org/content/10.1101/2022.02.10.479831v1

Classification: Physical Sciences/ Biophysics and Computational Biology

Key Words: Alpha-synuclein, amyloid fibrils, fibril polymorphism, alpha-synuclein monomer

Abstract

α-Synuclein inclusions are a pathological hallmark of several neurodegenerative diseases. Although it has been demonstrated a relationship between fibril polymorphism and different pathologies, the molecular origins of polymorphism are not understood. Employing biophysical approaches, we revealed that the conformational state of the monomeric αSyn is responsible for fibril polymorphism: αSyn adopts specific conformations at high NaCl that produce rod fibrils, and different conformations at low NaCl that generate twisted fibrils. Using NMR, we found that the high NaCl conformations establish a polar interaction between the initial part of the NAC region and a wide section of the C-terminus domain. These high NaCl conformations can be commonly promoted by changes in the chemical environment, like NaCl, the presence of Ca^{2+} or cellular components, like endotoxins, that alter the interaction NAC/C-terminus domain. Our results provide mechanistic insights that explain how the behavior of the C-terminus domain imparts polymorphism during the fibril formation.

Significance Statement

The accumulation of the protein α-Synuclein into amyloid aggregates in the brain is a key characteristic of neurodegenerative disorders like Parkinson's disease and multiple system atrophy. Intensive research has demonstrated that structurally different amyloid fibrils are related to the development of different diseases; however, the molecular mechanisms that originate such fibril diversity from the same protein remain unknown. In this work, we discovered that the conformational state of the monomeric αSyn, regulated by an intramolecular polar interaction NAC region/C-terminus domain, is crucial for the generation of different fibrils. Our results represent the monomeric molecular events behind the diversity of fibrils and open the conformational state of αSyn as a target to understand how the fibrils get formed in the brain.

Introduction

The accumulation of alpha-synuclein (αSyn) is a pathological hallmark of Parkinson's disease (PD) and multiple system atrophy (MSA) (Gai et al., 1998; Spillantini et al., 1998, 1997); however, although these synucleinopathies are produced by the same protein, they exhibit clinically distinctive features. Recently, we have developed experimental strategies to study directly the structural characteristics of inclusions in patient's brain employing Fourier-Transform Infrared microscopy (FTIR) and Small-Angle X-Ray Scattering (SAXS), proving that Lewy Bodies (LBs) contain cross β-sheet αSyn fibrils, while the amount of β-sheet structure in LBs and glial cell inclusions in MSA patients is different (Araki et al., 2020, 2019, 2015). These studies indicate that αSyn aggregates associated with PD and MSA correspond to different structural strains. Supporting our data, evidence corroborating distinctive strains in PD and MSA was provided analyzing amplified fibrils from the patients' brain using the protein misfolded cyclic amplification (PMCA) method (Shahnawaz et al., 2020; Van der Perren et al., 2020), and through the direct observation of accumulated fibrils in patient's brain by cryo-electron microscopy (Cryo-EM) (Schweighauser et al., 2020; Yang et al., 2022). Moreover, brain homogenates extracted from PD and MSA patients, as well as structurally different preformed fibrils, induced different cellular transmissibility, toxicity, membrane disruption, etc. (Fusco et al., 2017; Hayakawa et al., 2019; Peelaerts et al., 2018; Peng et al., 2018; Prusiner et al., 2015; Suzuki et al., 2020; Van der Perren et al., 2020; Yamasaki et al., 2019), leading to the hypothesis that pathological differences among synucleinopathies can be explained in terms of morphological variations in the accumulated αSyn fibrils in the brain (Brundin and Melki, 2017; Ikenaka et al., 2019). *In vitro*, different strains of αSyn fibrils can be produced when the fibrils are generated under conditions of low or high ionic strength, whose characteristics resemble some of the morphological properties of the fibrils observed in PD and MSA patients (Bousset et al., 2013; Peelaerts et al., 2018, 2015).

Despite the substantial progress in the analysis of strains extracted from patients' tissues and created *in vitro*, the molecular mechanisms that explain the origins of different strains from the same wild type αSyn remain poorly understood. To address this question, we focused on the conformational change of the monomeric αSyn. Several studies have reached a consensus about the disordered nature of αSyn (Bertoncini et al., 2005; Izawa et al., 2012; Kessler et al., 2003; Zhou et al., 2010); however, αSyn can also adopt some partially folded structures under acidic pH and high temperature (Furukawa et al., 2020; Ranjan and Kumar, 2017), or show different conformations in the presence or absence of salt (Bai et al., 2016). Furthermore, some groups have proposed that these conformations represent intermediate species during the formation of fibrils (Bai et al., 2016; Edwards and Reid, 2000; Morar et al., 2008; Ulrih et al., 2008). Nevertheless, it remains unclear whether these conformational variations exist in the physiological environment and what their relationship is to polymorphisms. In

this study, we propose that the molecular mechanisms responsible for polymorphism are linked to the monomeric conformational state. Changes in the monomeric conformation could potentially take place in the cell environment, events that might be related to the formation of specific morphologies in the brain.

Results

αSyn distinct fibril strains can be modulated by the conformational state of the monomer

Recently, it has been published the atomic level structure of the fibrils obtained by direct visualization of aggregates from patients using Cryo-EM (Schweighauser et al., 2020; Yang et al., 2022); however, this structural information alone is not enough to unveil the molecular mechanisms responsible of generating these specific morphologies. To understand how the diversity of fibrils are created, we propose to transfer the complex biological environment into a simple in vitro system in the test tube, in which the fibril diversity can be modulated with small molecules and be studied systematically. The simplicity of this model would allow the identification of the minimal molecular requirements and conditions needed to produce fibril polymorphism in vitro. To count with a reference for our in vitro fibrils, we propose the use of amplified fibrils from brain lysates as model. It is known that the amplification of fibrils from brain through PMCA strategies produces fibrils with distinct ultrastructure from the original seeds (Lövestam et al., 2021); however, these amplified fibrils also retain some of the structural elements and morphology of the original seeds (Shahnawaz et al., 2020). With this purpose, we amplified amyloid fibrils from PD and MSA patients' brain, using amygdalae homogenates as seeds. The presence of αSyn aggregates in the amygdalae for all the cases was confirmed by immunohistochemical analysis (**Figure S1.A**). We monitored the kinetics of fibril amplification by our HANABI assay (Kakuda et al., 2019; Nakajima et al., 2021) (**Figure S1.B**), and analyzed the morphological properties of the amplified fibrils by transmission electron microscopy (TEM, **Figure S1.C**). As previously reported (Shahnawaz et al., 2020), we observed that fibrils amplified from PD patients' brain exhibit a higher ThT intensity than those obtained from MSA. The microscopic visualization showed that PD-amplified fibrils are characterized by rod-like fibrils, with two parallelly aligned protofilaments; while MSA-derived fibrils depicted a twisted morphology, in which two protofilaments entangle over each other. Despite the limitations of the fibril amplification methods (Lövestam et al., 2021), the morphological differences detected in our model fibrils of PD and MSA diseases highlight the importance of a deeper investigation to reveal the molecular mechanisms responsible for polymorphism.

Previous reports have shown that different fibril morphologies, each one with distinctive biophysical and biochemical properties, can be generated in vitro employing low or high ionic strength

conditions (Bousset et al., 2013; Peelaerts et al., 2018, 2015). A deeper knowledge of the fibril morphology dependence in function of the concentration of NaCl would expand our understanding of the molecular events underlying the polymorphism of fibrils. Therefore, we examined the αSyn fibril formation by ThT assay in the presence of 50 mM TRIS pH 7.4 supplemented with 0 to 500 mM NaCl (**Figure 1.A**). Interestingly, below 300 mM NaCl, we found typical sigmoidal kinetic curves with relatively low maximal ThT intensity values (< 0.2 A. U.). At 300 mM NaCl, a wider distribution of curves with both low and high maximal ThT was detected, while above 400 mM NaCl, just fibrils with high values of ThT intensity were observed. To determine the behavior of the maximal ThT intensity of fibrils, we plotted the maximal values of ThT as a function of the concentration of NaCl, finding a region dominated by low maximal ThT values below 300 mM NaCl, and a region with high maximal ThT values above 300 mM. We defined the inflection point of the maximal ThT values as the concentration of NaCl, 300 mM, in which fibrils with both low and high ThT can be produced by chance. Moreover, we evaluated by TEM the morphological properties of the fibrils created at different concentrations of NaCl (**Figure 1.B,** upper and lower-right). First, it was found that the low-ThT fibrils obtained below 300 mM NaCl exhibit a twisted polymorph, while the fibrils produced above 300 mM showed a rod-like polymorph. In terms of morphology, the high and low salt created fibrils resemble some of the morphologic properties of the PD- and MSA-amplified fibrils.

In addition, we also confirmed by SDS-PAGE densitometry that the yield of both the low and high ThT fibrils created at low and high salt, respectively, is higher than 95 % (**Figure S2.A**), discarding the possibility of incomplete reactions or the lack of fibrillation products when low ThT is observed. Finally, we recorded the FTIR spectra of both low-salt and high-salt fibrils, finding in both cases typical bands of β-sheet structure around 1630 cm^{-1}, demonstrating the presence of amyloid fibrils in both NaCl conditions, and excluding the formation of amorphous aggregates (**Figure S2.B**). The deconvolution of the FTIR spectra showed that the contents of β-sheet structure is higher for the fibrils created at 50 mM NaCl, indicating structural differences between the fibrils (**Figure S2.C**).

For the biochemical characterization of fibrils, we developed a proteinase K resistance assay (PKR) to evaluate and compare the digestion patterns of fibrils with different morphologies. Considering the first five highest molecular weights in the proteolysis patterns after 60 minutes of reaction, rod-like fibrils showed a digestion profile with stronger band intensities for the second (B2) and fourth (B4) bands, and a high value of the ratio (B4/B5); while twisted fibrils presented a weaker B2 band and a low value of the ratio (B4/B5) (**Figure S2.D-E**). Employing this PKR assay, we evaluated the digestion patterns of fibrils obtained at 50 mM and 500 mM NaCl concentrations, where the differential digestion profiles for twisted and rod fibrils, respectively, were confirmed (**Figure 1.C**, left). Furthermore, we tested the PKR assay of selected fibrils created at 300 mM NaCl with low and

high maximal ThT fibrils, whose digestion patterns are in good agreement with the morphology visualized by TEM (**Figure 1.C**, right). Finally, we also evaluated the digestion patterns of fibrils amplified from PD and MSA brain samples, in which degradation profiles with similarities with the rod-like and twisted morphologies, respectively, were detected. We also observed a different bands pattern of B4 and B5 bands in MSA amplified fibrils, suggesting the existence of some distinctive elements at the ultrastructural level (**Figure S1.D**). Taken together, these results corroborated that the transition of maximal ThT values in function of the concentration of NaCl reflects the morphology salt dependence of the fibrils. The fibril diversity created here might be conceptually similar to the polymorphism originated by the effect of intracellular components.

We then explored the upstream molecular events that influence the salt dependence of fibril morphology. It has been reported previously that αSyn can adopt different conformational states in solution (Bai et al., 2016; Bertoncini et al., 2005; Furukawa et al., 2020; Zhou et al., 2010). In order to investigate whether these conformations are related to the molecular events in the early monomeric state that lead to the formation of specific fibrils, we started solving a solution of αSyn by analytical size exclusion chromatography (SEC) at 300 mM NaCl (**Figure 1.D,** upper). At this ionic strength, αSyn can produce both rod and twisted morphologies. Interestingly, the full-length αSyn monomer, whose molecular weight is 14.6 kDa, was observed as a single asymmetric peak, widely distributed in retention volume values ranging from molecular weights of 15 kDa to 60 kDa for hypothetical spherical-shaped globular proteins. The peak center of αSyn was observed around the retention volume that corresponds to 50 kDa globular proteins. This result suggests that αSyn monomers can adopt a variety of conformations in which the apparent hydrodynamic size changes. We confirmed by Western blotting that all the collected αSyn fractions separated by SEC consist of intact full-length monomers that have access to conformations with different hydrodynamic radii (**Figure 1.D**, lower). In addition, we also evaluated the retention volume of the monomeric αSyn between 0 and 500 mM NaCl, finding a tendency to increase the retention volume with the concentration of NaCl (**Figure 1.E** and **Figure S3.A**), suggesting that the monomers experience conformational changes upon the increase of the ionic strength. To discard the possibility that the changes observed by SEC could be attributed to nonspecific interactions between the column resin and the protein, we repeated the experiment in the presence of Poloxamer-188, a detergent that we have employed to reduce intermolecular interactions resin/protein (Kizuki et al., 2022; Maruno et al., 2021) (**Figure S3.B**). We found that the retention volume still increases with the NaCl concentration, indicating that the conformational change of αSyn is not an artifact of the interaction resin/protein. Moreover, we evaluated the retention volume of αSyn solutions in the presence of bovine serum albumin (BSA) as internal standard, at 150 mM and 500 mM NaCl (**Figure S3.C**). No variation in the retention volume of BSA (left peak) but only for

αSyn (right peak) was detected, corroborating that the changes in the retention volume observed at different conditions of ionic strength are specific for αSyn. Finally, to implement a simple method to estimate variations in the conformational state, we designed a filtration protocol employing filter units with a cut-off of 30 kDa, in which certain conformations would be able to cross the filter membrane while other would be retained (**Figure S3.D**). Therefore, we incubated monomeric αSyn with increasing NaCl concentrations, from 0 to 1000 mM, and measured by UV-spectroscopy the percentage of protein that could cross the membrane (**Figure 1.F**). We observed a constant increase in the percentage of protein that could cross the membrane until reaching a plateau phase above 300 mM NaCl, a behavior that resembles the SEC experiments. Taken together, both results of SEC and filtration suggest that the protein suffers conformational modifications upon the increase in NaCl concentration, that we classified into those conformations present in conditions that form twisted fibrils ($\text{Conf.}_{\text{LowSalt}}$) and those present in conditions that lead to rod-like fibrils ($\text{Conf.}_{\text{HighSalt}}$).

The behavior of the C-terminus determines the conformational change of αSyn

To determine the molecular nature of the monomeric conformational states of αSyn produced by salt, we employed different NaCl concentrations (0-500 mM) to record ^{1}H-^{15}N HSQC spectra (**Figure 2.A** and **Figure S4.A**). The analysis of the peak intensities as a function of NaCl concentration, using the spectrum obtained at 0 mM NaCl as reference, allowed us to detect a constant decrease in the peak intensity at the initial part of the NAC region and in the majority of residues in the C-terminus domain residues (**Figure 2.B** and **Figure S4.B**), detected by both difference ($Int_{[\text{NaCl}]} - Int_{[\text{NaCl}]=0}$) and ratio ($Int_{[\text{NaCl}]} / Int_{[\text{NaCl}]=0}$) of peak intensities. Additionally, some peaks disappeared upon the increase in NaCl concentration, located mostly in the NAC region (**Figure S4.B**, marked with gray bars). Remarkably, the peaks that experienced the most significant changes in the NAC domain were attributed to aliphatic and non-charged polar residues. Among the peaks showing changes in the C-terminus domain, half were attributed to aliphatic, aromatic, or non-charged polar residues, and the others to negatively charged residues (**Figure 2.C**). These results indicate that the $\text{Conf.}_{\text{HighSalt}}$ are constituted by monomers in which the initial part of the NAC region establishes intramolecular interactions with the C-terminus domain.

Finally, we evaluated the possibility of the formation of oligomers after the NMR spectra measurements by injecting a sample onto the analytical SEC column immediately after recording its HSQC spectrum (**Figure S4.C**), showing that the protein retains its monomeric state even after the incubation with high concentration of NaCl and the NMR experiments. Moreover, we recorded the far-UV CD spectroscopy of the monomeric solutions at 0 and 500 mM NaCl (**Figure S4.D**), indicating that in both cases, the protein depicts a disordered structure.

Additionally, we explored 576 structures deposited in the Protein Ensemble Data Bank, PED00024 (Allison et al., 2009) to corroborate the experimental HSQC spectra. In all the salt concentrations, the closest structure to our data, evaluated by the lowest root-mean-square (RMS), was an extended conformation (**Figure S4.E**, left). Interestingly, the second lowest RMS value at 500 mM NaCl had conformation with the C-terminus domain interacting with the central region of the protein (**Figure S4.E**, right), and the RMS value of this structure decreased as the salt concentration increased. These results are consistent with our experimental data that showed a conformational change when NaCl was added.

Calcium ions modulate the monomeric conformation and shift the inflection point of fibril morphologies to the rod fibril.

It has been reported that the biologically relevant cation Ca^{2+} binds to the negatively charged residues of the C-terminus domain, and alters the conformation of αSyn (Lautenschläger et al., 2018; Stephens et al., 2020). With this background, we assessed Ca^{2+} ions as modulators of the conformational state of αSyn. First, we examined the fibril formation in presence of 200 Eq. Ca^{2+} at different ionic strength, ranging from 21 to 500 mM (**Figure 3.A** and **Figure S5.A**). In the presence of Ca^{2+}, below 200 mM ionic strength (IS) a variety of ThT values was seen, while above 200 mM IS just high ThT fibrils were observed. These results indicate that calcium promotes the formation of fibrils with high ThT at lower IS, and even prevents the formation of exclusively low ThT fibrils at low IS. The morphology of the fibrils formed at an IS of 200 mM in the presence of Ca^{2+} was tested by TEM (**Figure 3.B**) and PKR (**Figure 3.C**), that confirmed the morphological properties of the rod fibrils. In order to verify the relationship between fibril morphology and monomeric conformation, we resolved solutions of αSyn in the presence and absence of 200 Eq. Ca^{2+} at an IS of 200 mM by SEC (**Figure 3.D**), finding a significant higher retention volume when calcium is present in the solution, and suggesting a connection between the rod morphology and the conformational state of the monomer.

To determine the residues affected in the monomeric conformation induced by calcium, we recorded the ^{1}H-^{15}N HSQC spectrum of αSyn in the presence of 200 Eq. Ca^{2+} at an ionic strength of 200 mM (**Figure 3.E**). We found that the effect of an IS of 200 mM on αSyn, using 0 mM NaCl as reference, can induce just mild variations in the initial part of the NAC region and the C-terminus domain (**Figure 3.F**, upper). On the other hand, the peak intensities of αSyn treated with Ca^{2+} at an IS of 200 mM, compared with 0 mM NaCl (**Figure 3.F**, lower), showed a more intense decrease in the initial part of the NAC region and the C-terminus domain. Remarkably, this result indicates that calcium induces specific structural variations in the initial part of the NAC region and the C-terminus

domain, enhancing the effect of an ionic strength of 200 mM NaCl until reaching levels similar to those observed at higher concentrations of salt. The contribution of calcium to the effect of the ionic strength can be found in **Figure S5.B-C**. These results also suggest structural similarities between the conformational change induced by calcium and $Conf._{HighSalt}$.

The cellular environment alters the conformational state of αSyn

It has been reported that different cellular environments and their components can promote the formation of specific polymorphs (Peng et al., 2018). One interesting case is observed during the bacterial dysregulation of the microbiome in the gut, phenomenon that has been related to the development of PD. The release of microbial membrane metabolites, like Lipopolysaccharides (LPS), could represent a crucial mediator of αSyn amyloidogenesis via the gut-brain axis (Bhattacharyya and Bhunia, 2021). In addition, it has also been reported that LPS can induce the acceleration of the aggregation and generate structurally different fibrils with a specific toxicity in cell systems and mice (Bhattacharyya et al., 2019; Kim et al., 2016). To investigate the effect of the bacterial cellular components in the conformational state of the monomeric αSyn, and fibril morphology, we designed an alternative purification protocol in which some bacterial elements remained in the protein preparation, namely IEX-αSyn. Our standard purification strategy of αSyn (see Materials and Methods section) includes SEC and reverse phase chromatography after ion exchange chromatography (IEX) as final steps to completely remove molecules with similar charge than αSyn. From this point, we will call this protein HPLC-αSyn. However, IEX-αSyn preparation lacks the final steps of purification in order to keep in the protein mixture some components of the bacterial environment. Then, we analyzed and compared the chromatograms of both standard αSyn (HPLC-αSyn) and IEX-αSyn by analytical SEC (**Figure 4.A**). The chromatograms show the presence of a component with small size (dashed circle) in the IEX-αSyn sample. We analyzed this component by analytical reverse phase chromatography, FTIR spectroscopy, and the detection of LPS through a Toxin Sensor Kit (GenScript) (**Figure S6.A**). This element was not retained by the reverse phase column since its retention volume was the same as the injection peak (4 min). The FTIR spectrum is characterized by two bands, between 1700 and 1500 cm^{-1}. We also found an LPS-reactive result using the Toxin Sensor Kit. To compare the characteristics of this component with LPS, we prepared a solution of LPS to be analyzed using the same strategy as done in **Figure S6.A** (**Figure S6.B**). In a similar way, we found that LPS is not retained by the reverse phase column, and it possesses two bands between 1700 and 1500 cm^{-1} in its FTIR spectrum, which, in both cases could correspond to the Amide I and Amide II of LPS (Barkleit et al., 2011); although the slightly different position of the bands between both samples may suggest some variations in the composition of carbohydrates moieties. Taken these

results together, the fraction of low molecular weight of **Figure 4.A** corresponds to LPS. Next, we analyzed both IEX-αSyn and HPLC-αSyn by analytical reverse phase chromatography (**Figure 4.B**). HPLC-αSyn (in black) showed just a single peak that corresponds to αSyn, but IEX-αSyn showed the non-retained LPS peak (F1), and the αSyn peak accompanied by additional smaller peaks (F2, F3, and F4), whose intensities suggest that their composition in the IEX-αSyn preparation does not exceed but a subtle percentage, even compared with the F1 peak. An analysis by FTIR and SDS-PAGE (**Figure S6.B** and **C**) suggests that these peaks have a proteinic nature. Taken together, these results show that most of the additional elements in IEX-αSyn corresponds to LPS.

In order to understand the effect of the bacterial elements in the fibril morphology, we monitored the formation of IEX-αSyn fibrils by ThT assay in 50 mM TRIS pH 7.4 supplemented with NaCl ranging from 0 to 500 mM and compared with the morphology profile obtained in the **Figure 1.B** for the HPLC-αSyn (**Figure 4.C**). The results indicate that the bacterial components induce a ThT inflection point at a lower ionic strength (~150 mM) than the observed for HPLC-αSyn (~300 mM). The morphological consequences become evident at 200 mM NaCl, condition in which IEX-αSyn forms a fibril with higher ThT that exhibits a typical rod-like morphology (**Figure 4.C**, red square), while pure αSyn produces a fibril with lower ThT and twisted polymorph (**Figure 4.C**, gray square). Since the LPS molecule was identified as the main bacterial component in IEX-αSyn, we prepared an artificial IEX-αSyn by adding LPS to HPLC-αSyn and tested the fibril morphology dependence on the ionic strength by ThT assay (**Figure 4.D**), finding a ThT inflection point of ~150 mM, in good agreement with the value determined for IEX-αSyn. The morphological differences produced by the change in the inflection point of morphologies were also corroborated by TEM at 300 mM NaCl, ionic strength in which LPS added αSyn shows a rod-like morphology and the HPLC-αSyn a twisted fibril (**Figure 4.D**, purple and black squares, respectively).

Next, we performed ^{1}H-^{15}N HSQC experiments to determine the residues affected by the presence of bacterial endotoxins in IEX-αSyn at an IS of 200 mM. As shown for the case of calcium, an IS of 200 mM induces mild variations in the initial part of the NAC region and the C-terminus domain (**Figure 4.F** and **H**, upper). Interestingly, the bacterial endotoxins present in IEX-aSyn were also able to induce a more intense decrease in the initial part of the NAC region and the C-terminus domain, suggesting the existence of an enhancing effect that leads to a conformational change promoted by endotoxins (**Figure 4.F**, lower), similar to the observed with calcium. Remarkably, using the artificial IEX-αSyn (HPLC-αSyn + LPS), the ^{1}H-^{15}N HSQC spectrum is very similar to that obtained for IEX-αSyn (**Figure 4.G**). The similarities are clearer if we consider the difference of peak intensities between the HPLC-aSyn treated with LPS and the spectrum observed at 0 mM NaCl

(**Figure 4.F**, lower), where the regions mostly affected by LPS are almost identical to those observed in IEX-αSyn (**Figure 4.H**, lower). The affected regions in the presence of bacterial endotoxins and IEX-αSyn indicate similar conformational changes to those observed in Conf.$_{HighSalt}$.

With these results, and those obtained in the presence of NaCl and calcium, we aimed to identify the residues commonly affected by all the conditions that lead to the Conf.$_{HighSalt}$ and produce rod fibrils. To do this, we evaluated the signal change of individual residues induced by all the conditions tested. For instance, in **Figure 5.A**, we show the signal changes of N65, Y136, and V63. In all the residues, we observed a NaCl concentration dependent decrease of the signal. The red line indicates the peak change observed at 300 mM NaCl, in which the inflection point of rod fibrils was observed. In some cases, like N65 and Y136, we observed that calcium, LPS and the bacterial endotoxins were able to promote a peak intensity change similar to the observed at higher concentrations of salt, despite the IS was 200 mM. These residues could be commonly involved in the conformational change required to generate rod fibrils. On the other hand, in residues like V63 the additives could not produce a change that surpassed the established threshold, indicating that these residues are not necessarily related to the monomeric conformational change. More generally, in the **Figure 5.B** it is depicted the peak intensity change of all the residues in all the conditions tested, where it can be seen that the presence of Ca^{2+}, LPS and bacterial endotoxins promotes an NMR peak intensity change, under physiological ionic strength (~200 mM), similar to the observed at salt concentrations above 300 mM; especially for the residues in the initial part of the NAC region and the C-terminus domain, for example, N65 and Y136 (**Figure 5.B**, red arrows). In order to systematically identify the residues involved in the formation of rod fibrils, we evaluated for all the residues whether the additives tested, in a physiological IS, produced a signal change higher or equal to 300 mM NaCl (**Figure S7**). This analysis let us recognize the residues commonly affected under all the tested conditions. An alignment comparing the most relevant changes is provided in **Figure 5.C.** The global analysis shows two main affected regions for all the cases: the initial part of the NAC region and a wide area of the C-terminus domain. Considering these results, it is clear that all the tested conditions share a common conformational change enhanced by the interaction between the initial part of the NAC region and the C-terminus domain that precedes the formation of rod fibrils. Thus, the interaction NAC/C-terminus domain is the characteristic that defines the Conf.$_{HighSalt}$ state.

The C-terminus domain is essential for the monomeric Conf.$_{HighSalt}$ and fibril polymorphism.

We have identified the C-terminus domain as a key factor for the Conf.$_{HighSalt}$ of the monomeric αSyn. If we examine the sequence of the C-terminus domain, we will find four aromatic residues: one

phenylalanine and three tyrosine residues. Among the tyrosine residues, two of them were directly identified by the global algorithm employed to analyze the NMR data (Y133 and Y136), suggesting that the chemical environment of the tyrosine residues could change upon the conformational changes of αSyn (**Figure S8.A**). Since the aromatic residues can be studied relatively easily with spectroscopic tools, we employed near-UV circular dichroism (CD) spectroscopy to evaluate the alterations in the tyrosine environment in the presence of components that induce the $Conf._{HighNaCl}$ of monomers, like high concentration of NaCl and calcium (**Figure S8.B**). The spectra showed some differences in the region of the tyrosine residues (265-285 nm), whose ellipticity values become less negative in conditions that promote $Conf._{HighSalt}$, while the phenylalanine residues region (255-265 nm) remained unaltered. These results indicate that spectroscopic tools that target the aromatic residues could be implemented as first approaches to detect the conformational changes in αSyn.

In order to demonstrate the intramolecular character of the interaction between the NAC region and the C-terminus domain, we designed, purified and analyzed a mutant of αSyn (**Figure 6.A**). Based on the global NMR analysis shown in the **Figure 5**, we detected that the residues Y133 and Y136 play a crucial role in the interaction between the NAC region and the C-terminus domain. Thus, we prepared a mutant with substitutions in Y133 and Y136 per alanine, with the additional mutation Y125A to reduce the global effect of the tyrosine residues in the C-terminus domain and inhibit $Conf._{HighSalt}$ and, consequently, the rod-like fibril morphology.

First, we analyzed the capacity of the tyrosine mutant Y125A/Y133A/Y136A-αSyn to form rod and twisted fibrils in a variety of ionic strength values in the presence of NaCl (**Figure 6.B**, left), 200 Eq. Ca^{2+} (**Figure 6.B**, middle), and LPS (**Figure 6.B**, right), finding that the triple mutant depicts low ThT values under all the ionic strength values. The morphological properties imaged by TEM (**Figure 6.C**) corroborated that the fibrils created at 400 mM ionic strength were characterized by a rod morphology for WT-αSyn with NaCl, but just twisted fibrils were observed for the Tyr-mutant in the presence of all the additives evaluated. These results suggest that the presence of NaCl, Ca^{2+} and LPS is not enough to induce the rod morphology if the intramolecular interaction responsible of the conformational change is disrupted.

The capability of the mutant to adopt the $Conf._{HighSalt}$ by NaCl was tested by SEC, where a resistance to change the retention volume in function of the concentration of NaCl was detected in the triple mutant (**Figure 6.D**, left, and **Figure S9.A**). To investigate if calcium promotes the conformational change of Y125A/Y133A/Y136A-αSyn, we analyzed both the triple tyrosine mutant and the WT αSyn in the presence and absence of 200 Eq. Ca^{2+} at 200 mM ionic strength (**Figure S9.B**). We found that the triple mutant, in the presence and absence of calcium, has lower retention volume

values than WT αSyn, which indicates a resistance of the triple mutant to adopt the Conf.$_{HighSalt}$ even with calcium (**Figure S9.B**). As observed in **Figure 3.D**, calcium led to an increase in the retention volume in the WT αSyn, produced by the compaction of the WT αSyn. However, calcium also induced a slight increase in the retention volume of the triple tyrosine mutant; therefore, we established the ratio R.V.$_{Ca}$/R.V.$_{NoCa}$. (R.V.$_{Ca}$= retention volume in the presence of calcium, R.V.$_{NoCa}$= retention volume in the absence of calcium) to evaluate how different is the effect of calcium on both proteins (**Figure 6.D**, right). R.V.$_{Ca}$/R.V.$_{NoCa}$ showed that calcium has a stronger effect on the WT-αSyn than on the triple mutant, which suggest that although the triple mutant offers a resistance to the compaction, it could still interact with calcium.

Next, we recorded the ^{1}H-^{15}N HSQC spectra of the triple mutant at different NaCl concentrations (0-500 mM) (**Figure 6.E, left** and **Figure S9.C**). The analysis of the peak intensities as a function of NaCl, using the spectrum obtained at 0 mM NaCl as reference, allowed us to see residues mildly affected in the initial part of the NAC region and the C-terminus domain. These changes in intensity did not vary more when the concentration of salt became higher, indicating that the intramolecular polar interaction between the NAC region and the C-terminus domain has been destabilized. In addition, the ratio $I_{[NaCl]= X}$ / $I_{[NaCl]= 0}$ indicates mild decreases in the NAC region and the C-terminus domain that did not get more affected with the concentration of salt (**Figure S9.D**). Additionally, we recorded the ^{1}H-^{15}N HSQC spectra of Y125A/Y133A/Y136A-αSyn at an ionic strength of 200 mM in the presence of 200 Eq. Ca^{2+} (**Figure 6.E, right,** and **Figure S9.E**). The peak intensities of Y125A/Y133A/Y136A-αSyn treated with Ca^{2+} compared with 0 mM NaCl (**Figure 6.E**, Right), showed a few small changes in the initial part of the NAC region and some decreases in intensity in the C-terminus domain, around the residues 120 and 130. Interestingly, the residues Q62 and N65, relevant for the compaction, did not show significant changes upon the addition of calcium. The NMR data suggest that the triple mutant protein still has the capability of binding calcium, probably through the C-terminus domain, but also indicate that the mutant cannot adopt the Conf.$_{HighSalt}$ because the polar interaction between C-terminus and NAC region got disrupted, which would explain why calcium cannot induce rod fibrils in the triple mutant. Taken together, the NMR results strengthen the conclusion that the intramolecular interaction NAC/C-terminus domain plays a key role in the generation of the rod morphology.

Finally, since a wide section of the C-terminus domain has been recognized as crucial for the conformational change of the monomeric αSyn, we examined a truncated form of αSyn that lacks this region, from E104 to A140, namely N103t-αSyn, (**Figure 7.A**). Previous studies have shown that C-terminus truncated αSyn variants are characterized by a faster aggregation, faster seeding effect, differential contents of β-sheet structure and twisted morphologies (Iyer et al., 2017; Liu et al., 2005;

Ni et al., 2019). In agreement with these reports, N103t-αSyn showed that the ThT values for all the fibrils were low, independently from the ionic strength (**Figure 7.B**). A TEM visualization of the fibrils showed that just twisted fibrils were detected, even at high concentrations of salt (**Figure 7.C**). Additionally, we evaluated if there were changes in retention volume by analytical SEC, however, the retention volume did not show any significant variation in the interval from 50 mM to 500 mM NaCl (**Figure 7.D**). These results indicate that the lack of the key region of the C-terminal domain is enough to prevent not just the formation of rod fibrils but also any variation in the conformational state of the monomeric N103t-αSyn.

Discussion

In this study, employing physicochemical approaches, we have found that, by the effect of NaCl, Ca^{2+} or LPS, αSyn can adopt the conformational state denominated $Conf._{HighSalt}$, which is related to the formation of the rod-like polymorph. NaCl, Ca^{2+} and LPS have a variety of effects in αSyn via the charge neutralization of the protein, changes in the hydration shell, amorphous aggregation, coordination of calcium, non-specific protein interactions, etcetera; however, we were able to determine, by NMR, the essential residues affected when αSyn acquires the $Conf._{HighSalt}$ state. Through the global analysis of the individual residues NMR change, we detected, for all the conditions, some common peak intensity variations in the initial part of the NAC region and the C-terminus domain, suggesting the existence of a polar interaction between these domains. To support this idea, we disrupted the polar interactions between the NAC region and the C-terminus domain by introducing mutations in all the tyrosine residues of the C-terminus domain by alanine. Importantly, the triple tyrosine mutant prevented the $Conf._{HighSalt}$ of the protein in all the tested conditions and led to the formation of twisted fibrils. From these results, we conclude that the conformational change mediated by tyrosine residues is the essential molecular event that leads to rod fibrils. The identification of the C-terminus domain as key factor for the $Conf._{HighSalt}$ is particularly remarkable since this region is the target of several modifications, like phosphorylation, cross-linking, ubiquitination, truncation, interaction with metals, etc. (Oueslati, 2016), events that could potentially affect the conformational state of αSyn and the consequent fibril morphology.

The simple modification of the ionic strength adjusting the NaCl concentration is enough to induce the $Conf._{HighSalt}$ and the formation of specific polymorphs *in vitro*, however, it is unlikely to find such conditions of high ionic strength in the living cell. The study of biologically relevant molecules, like calcium and LPS, acquires a crucial importance since these molecules can recreate the $Conf._{HighSalt}$ in a milder ionic strength. A careful analysis of our NMR data allowed us to propose

mechanisms that promote the interaction of the initial part of the NAC region with the C-terminus domain induced by Ca^{2+} and LPS. For calcium, it has been reported that it accelerates the speed of fibril formation, but also that it can interact with the negative residues of the C-terminus domain and disrupt the electrostatic contacts with the positively charged N-terminus domain (Lautenschläger et al., 2018; Stephens et al., 2020). Considering our results and the previous reports, we propose that Ca^{2+} partially titrates the negative charges of the C-terminus domain, promoting polar interactions between the C-terminus domain and the initial part of the NAC region, leading to the $Conf._{HighSalt}$ in the physiological range of ionic strength. For LPS, a molecule associated with the amyloidogenesis of αSyn through the gut-brain axis (Bhattacharyya and Bhunia, 2021), it has been reported that, in the micellar form, it establishes contacts with αSyn through the N-terminus, the NAC region and a few residues of the C-terminus domain (Bhattacharyya et al., 2019). In the presence of LPS, our NMR experiments could also detect variations in the N-terminus domain and some hydrophobic residues of the NAC region of αSyn. With these results, we propose a mechanism of conformational change via LPS: when LPS binds the N-terminus domain and some residues of the NAC region, the interaction between the initial part of the NAC domain and the C-terminus domain gets facilitated, leading to the formation of the $Conf._{HighSalt}$ bound to LPS, which is able to produce rod fibrils at lower ionic strength.

Interestingly, it has been reported the existence of an autoinhibitory form of αSyn, resistant to aggregation, produced by the electrostatic interaction between the N- and C-terminus domains (Bertoncini et al., 2005). The autoinhibitory form has been disrupted in the presence of polyamines (Bertoncini et al., 2005), but also with calcium (Stephens et al., 2020). In both cases, the disruption involves the interaction with the C-terminus domain to release the protein from this state, but the following molecular events that generates fibrils remained unknown. Considering our findings, we hypothesize that the autoinhibitory forms of αSyn would get disrupted by high NaCl, Ca, LPS, or other additives, and adopt the polar interaction between C-terminus domain and the NAC domain to generate rod fibrils.

Molecules like Ca^{2+} and LPS represent good examples of how alterations in key metabolites could affect the formation of specific fibrils in the biological context; but the dysregulation of other crucial cell components, like lipids, might alter the conformation of αSyn monomers and promote the formation of specific polymorphs, like those observed in our PD- and MSA-derived fibril models. The model of the monomeric conformational change could be expanded to the complexity of the cellular environments. For instance, Peng *et al* (Peng et al., 2018) reported that the αSyn aggregates in the neuronal cells can produce PD-like aggregates, whereas the αSyn aggregated in the oligodendrocyte resembles the MSA-like ones. Further investigation is required to determine the factors that induce conformational changes in the monomers and trigger the aggregation in the environments of the

neuronal cells and the oligodendrocytic cells. This knowledge would provide insights to better understand the pathogenesis of each alpha synucleinopathies.

Finally, although our model of conformational change allows the prediction of fibril morphologies, the direct link explaining how the monomeric conformation and fibril morphology are related remains unsolved. Considering our results and the previously reported cryo-EM polymorphs structures for fibrils created *in vitro* (Guerrero-Ferreira et al., 2018; Li et al., 2018), we noticed that the Conf.$_{HighSalt}$ might constraint the formation of specific polymorphisms: 1) (**Figure S10. A**) at low ionic strength, the monomer adopts an ensemble of extended conformations with structural fluctuations. During the fibril formation, the structural monomeric plasticity allows the protein to acquire the most stable morphology: the twisted fibril. The driving force of the twisted fibril would be the protection from the solvent of the hydrophobic residues of the NAC region at the interface of the constituting protofilaments. 2) (**Figure S10.B**) Under conditions that promote the Conf.$_{HighSalt}$, the C-terminus domain that interacts with the initial part of the NAC region would protect the hydrophobic residues of this domain, preventing the hydrophobic contact between the protofilament interfaces required for the twisted fibril. Instead, an interface characterized by the electrostatic interaction between H50 and E57 and a hydrophobic zipper from G51 to A56 would be stabilized, leading to the formation of the rod fibril.

In this study, we have obtained evidence that suggests the importance of the monomeric conformational state in the morphology of the final mature fibrils, and how different molecules can recreate specific environments that favor certain conformations and morphologies. We have also proposed hypothetical molecular mechanisms that follow to the changes in the conformational state and that could explain the formation of specific polymorphs. Certainly, further investigation is required to determine experimentally how the protein in low salt and high salt conformations adopt the final structures reported by CryoEM. Also, our study offers molecular insights for the formation of rod fibrils but the molecular events that generate the twisted fibril remain elusive. In addition, we recognize that although our simple system provides the Conf.$_{HighSalt}$ as the minimal molecular requirement to generate rod fibrils, the effect of the real complex physiological environment must be incorporated in our model to understand the role of the conformational state and its relationship with the polymorphism in the living cell. To overcome this limitation, the conformational state of the monomeric αSyn can be targeted in future studies to evaluate how the protein structure evolves in the cell, which cellular environments and events trigger a specific conformation, how to prevent the formation of specific conformations, etcetera. This knowledge will let us better understand how the PD, DLB and MSA fibrils are created in the complex environment of the brain.

Materials and Methods

Assays of αSyn solutions. Expression and purification of human WT αSyn and its mutants are described in Supplementary Materials. Solutions of αSyn in the presence and absence of additives were analyzed by several methods including SEC, filtration assay, ^{1}H-^{15}N HSQC, reverse phase chromatography and CD. The details are described in Supplementary Materials

Assays of αSyn fibrils. The formation and morphology of fibrils were characterized by various methods including ThT fluorescence, TEM, FTIR, and PKR. The details are described in Supplementary Materials

Acknowledgments

We would like to thank Shizuka Sonoda and Miki Yoshida for the protein expression and purification and the excellent technical support received. CA thanks JSPS (postdoctoral fellowship P16388) for the financial support.

Funding: This work was supported by JSPS KAKENHI Grant JP16H06277, JP18H02741, 22K07516, 22H02951, 22K15643; JST CREST Grant Numbers JPMJCR18H4 and JPMJCR17H6; JSPS Core-to-Core Program A Advance Research Networks; AMED Grant Numbers JP18dm0107103, JP19dm0207001, JP20dm0107106, JP20dm0107158, JP20km0405206, JP20am0101110 and SENTAN16809202; and the Ministry of Education, Culture, Sports, Science and Technology Grant Number 17H06352. The Brain Mapping by Integrated Neuroethologies for Disease Studies (Brain/MINDS) from Japan Agency for Medical Research and development, AMED JP18dm0207020, JP22dm0207070. CA was funded by JSPS KAKENHI Grant 16F16388.

Author contributions: CA, KI, YG, and HM designed the experiments. CA, KI, MS, TM, KY, KN, CJC, KN, GB, KT, YY, JD, TM, MM, KK, MH, TA, NW, SB, YK, SM and YM performed the experiments. CA and KI analyzed the data. CA and KI wrote the original draft. MS, YK, SN, KB, HO, YN, YK, SU, YM, YG and HM reviewed the manuscript.

Competing interests: Authors declare no conflicts of interest.

Dedications: We would like to express our deep gratitude to Professor Kazuhiro Ikenaka for his support, precious advices, and discussions.

References

Allison JR, Varnai P, Dobson CM, Vendruscolo M. 2009. Determination of the free energy landscape of α-synuclein using spin label nuclear magnetic resonance measurements. *J Am Chem Soc*. doi:10.1021/ja904716h

Araki K, Yagi N, Aoyama K, Choong CJ, Hayakawa H, Fujimura H, Nagai Y, Goto Y, Mochizuki H. 2019. Parkinson's disease is a type of amyloidosis featuring accumulation of amyloid fibrils of α-synuclein. *Proc Natl Acad Sci U S A* **116**:17963–17969. doi:10.1073/pnas.1906124116

Araki K, Yagi N, Ikemoto Y, Hayakawa H, Fujimura H, Moriwaki T, Nagai Y, Murayama S, Mochizuki H. 2020. The secondary structural difference between Lewy body and glial cytoplasmic inclusion in autopsy brain with synchrotron FTIR micro-spectroscopy. *Sci Rep* **10**:1–6. doi:10.1038/s41598-020-76565-6

Araki K, Yagi N, Ikemoto Y, Yagi H, Choong CJ, Hayakawa H, Beck G, Sumi H, Fujimura H, Moriwaki T, Nagai Y, Goto Y, Mochizuki H. 2015. Synchrotron FTIR micro-spectroscopy for structural analysis of Lewy bodies in the brain of Parkinson's disease patients. *Sci Rep* **5**:1–8. doi:10.1038/srep17625

Arosio P, Knowles TPJ, Linse S. 2015. On the lag phase in amyloid fibril formation. *Phys Chem Chem Phys* **17**:7606–7618. doi:10.1039/C4CP05563B

Bai J, Cheng K, Liu M, Li C. 2016. Impact of the α-Synuclein Initial Ensemble Structure on Fibrillation Pathways and Kinetics. *J Phys Chem B* **120**:3140–3147. doi:10.1021/acs.jpcb.6b01225

Barkleit A, Foerstendorf H, Li B, Rossberg A, Moll H, Bernhard G. 2011. Coordination of uranium(vi) with functional groups of bacterial lipopolysaccharide studied by EXAFS and FT-IR spectroscopy. *Dalt Trans* **40**:9868–9876. doi:10.1039/c1dt10546a

Bertoncini CW, Jung YS, Fernandez CO, Hoyer W, Griesinger C, Jovin TM, Zweckstetter M. 2005. Release of long-range tertiary interactions potentiates aggregation of natively unstructured α-synuclein. *Proc Natl Acad Sci U S A* **102**:1430–1435. doi:10.1073/pnas.0407146102

Bhattacharyya D, Bhunia A. 2021. Gut-Brain axis in Parkinson's disease etiology: The role of lipopolysaccharide. *Chem Phys Lipids* **235**:105029. doi:https://doi.org/10.1016/j.chemphyslip.2020.105029

Bhattacharyya D, Mohite GM, Krishnamoorthy J, Gayen N, Mehra S, Navalkar A, Kotler SA, Ratha BN, Ghosh A, Kumar R, Garai K, Mandal AK, Maji SK, Bhunia A. 2019. Lipopolysaccharide from Gut Microbiota Modulates α-Synuclein Aggregation and Alters Its Biological Function. *ACS Chem Neurosci* **10**:2229–2236. doi:10.1021/acschemneuro.8b00733

Bousset L, Pieri L, Ruiz-Arlandis G, Gath J, Jensen PH, Habenstein B, Madiona K, Olieric V, Böckmann A, Meier BH, Melki R. 2013. Structural and functional characterization of two alpha-synuclein strains. *Nat Commun* **4**:2575. doi:10.1038/ncomms3575

Brundin P, Melki R. 2017. Prying into the Prion Hypothesis for Parkinson's Disease. *J Neurosci* **37**:9808–9818. doi:10.1523/JNEUROSCI.1788-16.2017

Delaglio F, Grzesiek S, Vuister GW, Zhu G, Pfeifer J, Bax A. 1995. NMRPipe: A multidimensional spectral processing system based on UNIX pipes. *J Biomol NMR* **6**:277–293. doi:10.1007/BF00197809

Edwards AJ, Reid D. 2000. Introduction to NMR of Proteins. *Curr Protoc Protein Sci* **19**:Unit 17.5. doi:10.1002/0471140864.ps1705s19

El Turk F, De Genst E, Guilliams T, Fauvet B, Hejjaoui M, Di Trani J, Chiki A, Mittermaier A, Vendruscolo M, Lashuel HA, Dobson CM. 2018. Exploring the role of post-translational

modifications in regulating α-synuclein interactions by studying the effects of phosphorylation on nanobody binding. *Protein Sci* **27**:1262–1274. doi:10.1002/pro.3412

Furukawa K, Aguirre C, So M, Sasahara K, Miyanoiri Y, Sakurai K, Yamaguchi K, Ikenaka K, Mochizuki H, Kardos J, Kawata Y, Goto Y. 2020. Isoelectric point-amyloid formation of α-synuclein extends the generality of the solubility and supersaturation-limited mechanism. *Curr Res Struct Biol* **2**:35–44. doi:10.1016/j.crstbi.2020.03.001

Fusco G, Chen SW, Williamson PTF, Cascella R, Perni M, Jarvis JA, Cecchi C, Vendruscolo M, Chiti F, Cremades N, Ying L, Dobson CM, De Simone A. 2017. Structural basis of membrane disruption and cellular toxicity by α-synuclein oligomers. *Science (80-)* **358**:1440–1443. doi:10.1126/science.aan6160

Gai WP, Power JHT, Blumbergs PC, Blessing WW. 1998. Multiple-system atrophy: A new α-synuclein disease? *Lancet*. doi:10.1016/S0140-6736(05)79256-4

Gasteiger E, Gattiker A, Hoogland C, Ivanyi I, Appel RD, Bairoch A. 2003. ExPASy: The proteomics server for in-depth protein knowledge and analysis. *Nucleic Acids Res* **31**:3784–3788. doi:10.1093/nar/gkg563

Guerrero-Ferreira R, Taylor NM, Mona D, Ringler P, Lauer ME, Riek R, Britschgi M, Stahlberg H. 2018. Cryo-EM structure of alpha-synuclein fibrils. *Elife* **7**:1–18. doi:10.7554/eLife.36402

Hayakawa H, Nakatani R, Ikenaka K, Aguirre C, Choong CJ, Tsuda H, Nagano S, Koike M, Ikeuchi T, Hasegawa M, Papa SM, Nagai Y, Mochizuki H, Baba K. 2019. Structurally distinct α-synuclein fibrils induce robust parkinsonian pathology. *Mov Disord* 1–12. doi:10.1002/mds.27887

Ikenaka K, Suzuki M, Mochizuki H, Nagai Y. 2019. Lipids as Trans-Acting Effectors for α-Synuclein in the Pathogenesis of Parkinson's Disease. *Front Neurosci* **13**:1–9. doi:10.3389/fnins.2019.00693

Iyer A, Roeters SJ, Kogan V, Woutersen S, Claessens MMAE, Subramaniam V. 2017. C-Terminal Truncated α-Synuclein Fibrils Contain Strongly Twisted β-Sheets. *J Am Chem Soc* **139**:15392–15400. doi:10.1021/jacs.7b07403

Izawa Y, Tateno H, Kameda H, Hirakawa K, Hato K, Yagi H, Hongo K, Mizobata T, Kawata Y. 2012. Role of C-terminal negative charges and tyrosine residues in fibril formation of α-synuclein. *Brain Behav* **2**:595–605. doi:10.1002/brb3.86

Kakuda K, Ikenaka K, Araki K, So M, Aguirre C, Kajiyama Y, Konaka K, Noi K, Baba K, Tsuda H, Nagano S, Ohmichi T, Nagai Y, Tokuda T, El-Agnaf OMA, Ogi H, Goto Y, Mochizuki H. 2019. Ultrasonication-based rapid amplification of α-synuclein aggregates in cerebrospinal fluid. *Sci Rep* **9**:6001. doi:10.1038/s41598-019-42399-0

Kessler JC, Rochet JC, Lansbury PT. 2003. The N-terminal repeat domain of α-synuclein inhibits β-sheet and amyloid fibril formation. *Biochemistry* **42**:672–678. doi:10.1021/bi020429y

Kim C, Lv G, Lee JS, Jung BC, Masuda-Suzukake M, Hong CS, Valera E, Lee HJ, Paik SR, Hasegawa M, Masliah E, Eliezer D, Lee SJ. 2016. Exposure to bacterial endotoxin generates a distinct strain of α-synuclein fibril. *Sci Rep* **6**. doi:10.1038/srep30891

Kizuki S, Wang Z, Torisu T, Yamauchi S, Uchiyama S. 2022. Relationship between aggregation of therapeutic proteins and agitation parameters: Acceleration and frequency. *J Pharm Sci* **000**:1–14. doi:10.1016/j.xphs.2022.09.022

Lautenschläger J, Stephens AD, Fusco G, Ströhl F, Curry N, Zacharopoulou M, Michel CH, Laine R, Nespovitaya N, Fantham M, Pinotsi D, Zago W, Fraser P, Tandon A, St George-Hyslop P, Rees E, Phillips JJ, De Simone A, Kaminski CF, Schierle GSK. 2018. C-terminal calcium binding of α-synuclein modulates synaptic vesicle interaction. *Nat Commun* **9**.

doi:10.1038/s41467-018-03111-4

Lee W, Rahimi M, Lee Y, Chiu A. 2021. POKY: a software suite for multidimensional NMR and 3D structure calculation of biomolecules. *Bioinformatics* **37**:3041–3042. doi:10.1093/bioinformatics/btab180

Lee W, Tonelli M, Markley JL. 2015. NMRFAM-SPARKY: Enhanced software for biomolecular NMR spectroscopy. *Bioinformatics* **31**:1325–1327. doi:10.1093/bioinformatics/btu830

Li B, Ge P, Murray KA, Sheth P, Zhang M, Nair G, Sawaya MR, Shin WS, Boyer DR, Ye S, Eisenberg DS, Zhou ZH, Jiang L. 2018. Cryo-EM of full-length α-synuclein reveals fibril polymorphs with a common structural kernel. *Nat Commun* **9**:3609. doi:10.1038/s41467-018-05971-2

Liu CW, Giasson BI, Lewis KA, Lee VM, DeMartino GN, Thomas PJ. 2005. A precipitating role for truncated α-synuclein and the proteasome in α-synuclein aggregation: Implications for pathogenesis of parkinson disease. *J Biol Chem* **280**:22670–22678. doi:10.1074/jbc.M501508200

Lövestam S, Schweighauser M, Matsubara T, Murayama S, Tomita T, Ando T, Hasegawa K, Yoshida M, Tarutani A, Hasegawa M, Goedert M, Scheres SHW. 2021. Seeded assembly in vitro does not replicate the structures of α-synuclein filaments from multiple system atrophy. *FEBS Open Bio* **11**:999–1013. doi:10.1002/2211-5463.13110

Maruno T, Usami K, Ishii K, Torisu T, Uchiyama S. 2021. Comprehensive Size Distribution and Composition Analysis of Adeno-Associated Virus Vector by Multiwavelength Sedimentation Velocity Analytical Ultracentrifugation. *J Pharm Sci* **110**:3375–3384. doi:10.1016/j.xphs.2021.06.031

Morar AS, Olteanu A, Young GB, Pielak GJ. 2008. Solvent-induced collapse of α-synuclein and acid-denatured cytochrome c. *Protein Sci* **10**:2195–2199. doi:10.1110/ps.24301

Nakajima K, Nishioka D, Hirao M, So M, Goto Y, Ogi H. 2017. Drastic acceleration of fibrillation of insulin by transient cavitation bubble. *Ultrason Sonochem* **36**:206–211. doi:10.1016/j.ultsonch.2016.11.034

Nakajima K, Noi K, Yamaguchi K, So M, Ikenaka K, Mochizuki H, Ogi H, Goto Y. 2021. Optimized sonoreactor for accelerative amyloid-fibril assays through enhancement of primary nucleation and fragmentation. *Ultrason Sonochem* **73**:105508. doi:10.1016/j.ultsonch.2021.105508

Narhi L, Wood SJ, Steavenson S, Jiang Y, Wu GM, Anafi D, Kaufman S a, Martin F, Sitney K, Denis P, Louis JC, Wypych J, Biere a L, Citron M. 1999. Both familial Parkinson's disease mutations accelerate alpha-synuclein aggregation. *J Biol Chem* **274**:9843–9846. doi:10.1074/jbc.274.14.9843

Ni X, McGlinchey RP, Jiang J, Lee JC. 2019. Structural Insights into α-Synuclein Fibril Polymorphism: Effects of Parkinson's Disease-Related C-Terminal Truncations. *J Mol Biol* **431**:3913–3919. doi:10.1016/j.jmb.2019.07.001

Oueslati A. 2016. Implication of Alpha-Synuclein Phosphorylation at S129 in Synucleinopathies: What Have We Learned in the Last Decade? *J Parkinsons Dis* **6**:39–51. doi:10.3233/JPD-160779

Peelaerts W, Bousset L, Baekelandt V, Melki R. 2018. α-Synuclein strains and seeding in Parkinson's disease, incidental Lewy body disease, dementia with Lewy bodies and multiple system atrophy: similarities and differences. *Cell Tissue Res* **373**:195–212. doi:10.1007/s00441-018-2839-5

Peelaerts W, Bousset L, Van der Perren A, Moskalyuk A, Pulizzi R, Giugliano M, Van den Haute C,

Melki R, Baekelandt V. 2015. α-Synuclein strains cause distinct synucleinopathies after local and systemic administration. *Nature* **522**:340–344. doi:10.1038/nature14547

Peng C, Gathagan RJ, Covell DJ, Medellin C, Stieber A, Robinson JL, Zhang B, Pitkin RM, Olufemi MF, Luk KC, Trojanowski JQ, Lee VM-Y. 2018. Cellular milieu imparts distinct pathological α-synuclein strains in α-synucleinopathies. *Nature* 1. doi:10.1038/s41586-018-0104-4

Prusiner SB, Woerman AL, Mordes DA, Watts JC, Rampersaud R, Berry DB, Patel S, Oehler A, Lowe JK, Kravitz SN, Geschwind DH, Glidden D V., Halliday GM, Middleton LT, Gentleman SM, Grinberg LT, Giles K. 2015. Evidence for α-synuclein prions causing multiple system atrophy in humans with parkinsonism. *Proc Natl Acad Sci U S A*. doi:10.1073/pnas.1514475112

Ranjan P, Kumar A. 2017. Perturbation in Long-Range Contacts Modulates the Kinetics of Amyloid Formation in α-Synuclein Familial Mutants. *ACS Chem Neurosci* **8**:2235–2246. doi:10.1021/acschemneuro.7b00149

Schweighauser M, Shi Y, Tarutani A, Kametani F, Murzin AG, Ghetti B, Matsubara T, Tomita T, Ando T, Hasegawa K, Murayama S, Yoshida M, Hasegawa M, Scheres SHW, Goedert M. 2020. Structures of α-synuclein filaments from multiple system atrophy. *Nature* **585**:464–469. doi:10.1038/s41586-020-2317-6

Shahnawaz M, Mukherjee A, Pritzkow S, Mendez N, Rabadia P, Liu X, Hu B, Schmeichel A, Singer W, Wu G, Tsai AL, Shirani H, Nilsson KPR, Low PA, Soto C. 2020. Discriminating α-synuclein strains in Parkinson's disease and multiple system atrophy. *Nature* **578**:273–277. doi:10.1038/s41586-020-1984-7

Shen Y, Bax A. 2010. SPARTA+: A modest improvement in empirical NMR chemical shift prediction by means of an artificial neural network. *J Biomol NMR*. doi:10.1007/s10858-010-9433-9

Spillantini MG, Crowther RA, Jakes R, Hasegawa M, Goedert M. 1998. α-Synuclein in filamentous inclusions of Lewy bodies from Parkinson's disease and dementia with Lewy bodies. *Proc Natl Acad Sci U S A*. doi:10.1073/pnas.95.11.6469

Spillantini MG, Schmidt ML, Lee VM, Trojanowski JQ, Jakes R, Goedert M. 1997. Alpha-synuclein in Lewy bodies. *Nature* **388**:839–840. doi:10.1038/42166

Stephens AD, Zacharopoulou M, Moons R, Fusco G, Seetaloo N, Chiki A, Woodhams PJ, Mela I, Lashuel HA, Phillips JJ, De Simone A, Sobott F, Schierle GSK. 2020. Extent of N-terminus exposure of monomeric alpha-synuclein determines its aggregation propensity. *Nat Commun* **11**. doi:10.1038/s41467-020-16564-3

Suzuki G, Imura S, Hosokawa M, Katsumata R, Nonaka T, Hisanaga SI, Saeki Y, Hasegawa M. 2020. α-synuclein strains that cause distinct pathologies differentially inhibit proteasome. *Elife*. doi:10.7554/eLife.56825

Ulrih NP, Barry CH, Fink AL. 2008. Impact of Tyr to Ala mutations on α-synuclein fibrillation and structural properties. *Biochim Biophys Acta - Mol Basis Dis* **1782**:581–585. doi:10.1016/j.bbadis.2008.07.004

Van der Perren A, Gelders G, Fenyi A, Bousset L, Brito F, Peelaerts W, Van den Haute C, Gentleman S, Melki R, Baekelandt V. 2020. The structural differences between patient-derived α-synuclein strains dictate characteristics of Parkinson's disease, multiple system atrophy and dementia with Lewy bodies. *Acta Neuropathol*. doi:10.1007/s00401-020-02157-3

Yagi H, Kusaka E, Hongo K, Mizobata T, Kawata Y. 2005. Amyloid fibril formation of α-synuclein is accelerated by preformed amyloid seeds of other proteins: Implications for the mechanism of transmissible conformational diseases. *J Biol Chem* **280**:38609–38616.

doi:10.1074/jbc.M508623200

Yamasaki TR, Holmes BB, Furman JL, Dhavale DD, Su BW, Song ES, Cairns NJ, Kotzbauer PT, Diamond MI. 2019. Parkinson's disease and multiple system atrophy have distinct -synuclein seed characteristics. *J Biol Chem*. doi:10.1074/jbc.RA118.004471

Yang Y, Shi Y, Schweighauser M, Zhang X, Kotecha A, Murzin AG, Garringer HJ, Cullinane PW, Saito Y, Foroud T, Warner TT, Hasegawa K, Vidal R, Murayama S, Revesz T, Ghetti B, Hasegawa M, Lashley T, Scheres SHW, Goedert M. 2022. Structures of alpha-synuclein filaments from human brains with Lewy pathology. *Nature*. doi:10.1038/s41586-022-05319-3

Zhou W, Long C, Reaney SH, Di Monte DA, Fink AL, Uversky VN. 2010. Methionine oxidation stabilizes non-toxic oligomers of α-synuclein through strengthening the auto-inhibitory intra-molecular long-range interactions. *Biochim Biophys Acta - Mol Basis Dis* **1802**:322–330. doi:10.1016/j.bbadis.2009.12.004

Figures

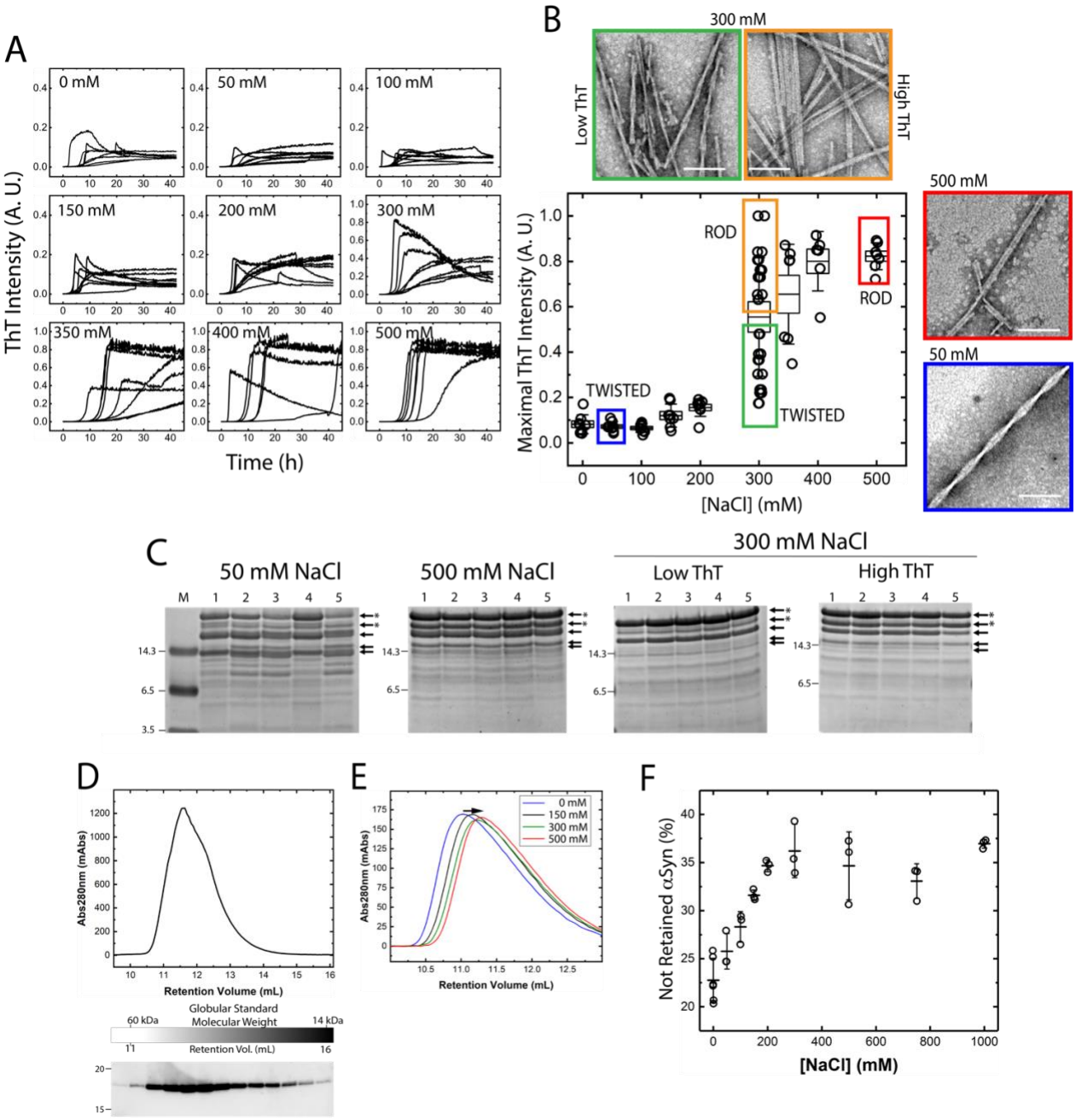

Figure 1. αSyn fibril morphology is modulated by the conformational state of the monomeric αSyn. (A) ThT-monitored αSyn fibril formation at different concentrations of NaCl. **(B)** Maximal ThT intensity values of fibrils created under the indicated concentration of NaCl. Boxes represent standard error of the mean values; whiskers represent standard deviation. Representative amyloid fibrils obtained at 50 mM (low ThT, blue square), 300 mM (low ThT, green square; high ThT, orange square) and 500 mM (red square) were visualized by TEM. (Bar scale: 200 nm). **(C)** From left to right, proteinase-K resistance assay of five replicates (numbers 1-5) of fibrils produced at 50 mM, 500 mM, created at 300 mM NaCl with maximal low- or high-ThT values, and amplified from PD and MSA brain of patients. Arrows indicate five selected bands subjected to intensity analysis. Bands marked with (*) denote the most relevant differences. Molecular weight markers (kDa) are shown on the left of each panel. **(D)** A solution of αSyn in 50 mM TRIS pH 7.4 supplemented with 300 mM NaCl was resolved by SEC (upper) and the fractions obtained were analyzed by Western Blotting (Anti-Syn211, lower). **(E)** Representative chromatograms of Solutions of monomeric αSyn at different concentrations of NaCl resolved by Size Exclusion Chromatography. **(F)** Percentage of αSyn monomers not retained by 30 kDa cut-off membrane, in function of NaCl.

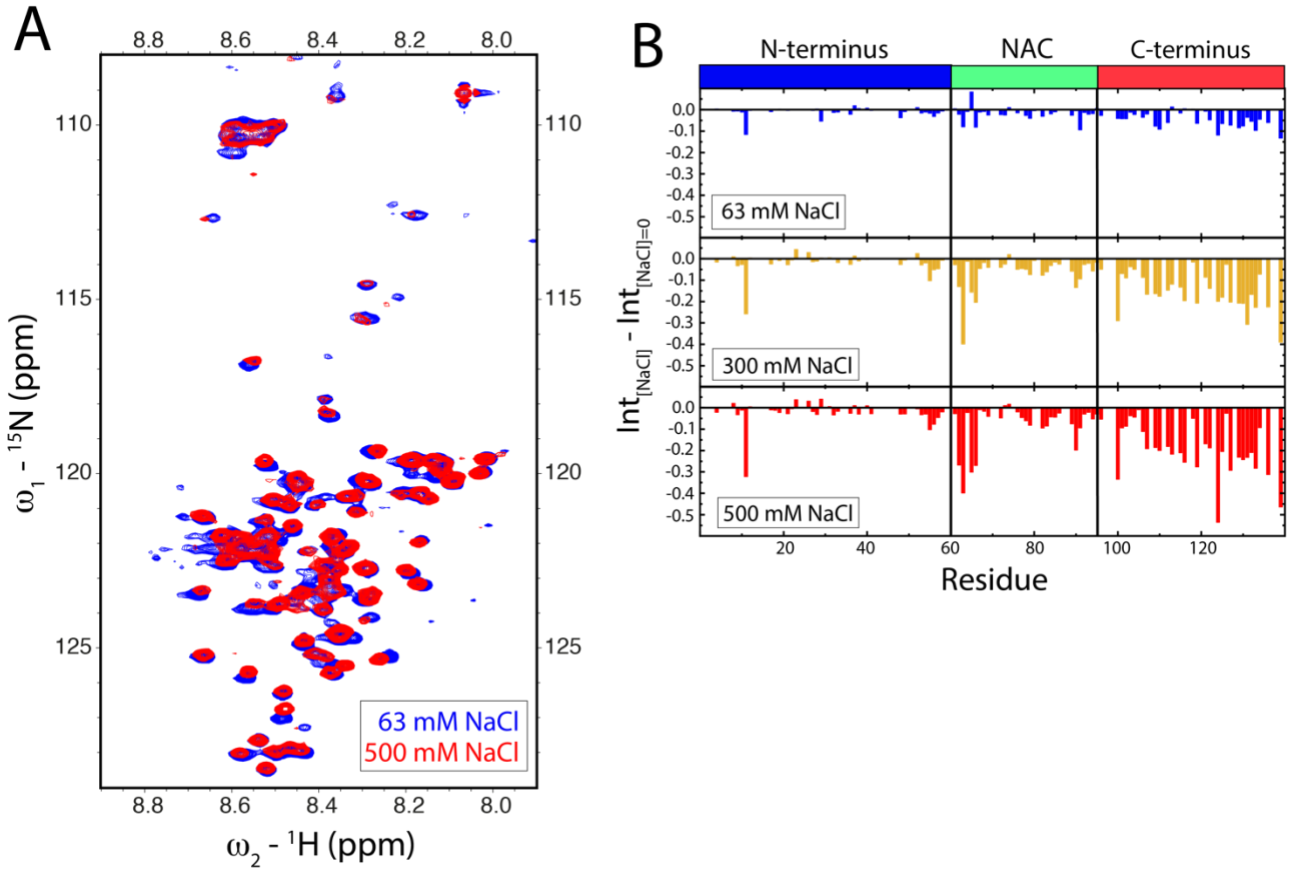

Figure 2. Compact αSyn monomers establish interactions between the C-terminus domain and NAC region. (A) ^{1}H-^{15}N HSQC spectra of solutions of αSyn supplemented with 63 mM (blue) and 500 mM (red) NaCl. **(B)** Peak intensity difference analysis of the spectra of αSyn of the amide N-H nuclei recorded at 63 mM, 300 mM, and 500 mM NaCl, employing the spectrum obtained at 0 mM NaCl as a reference.

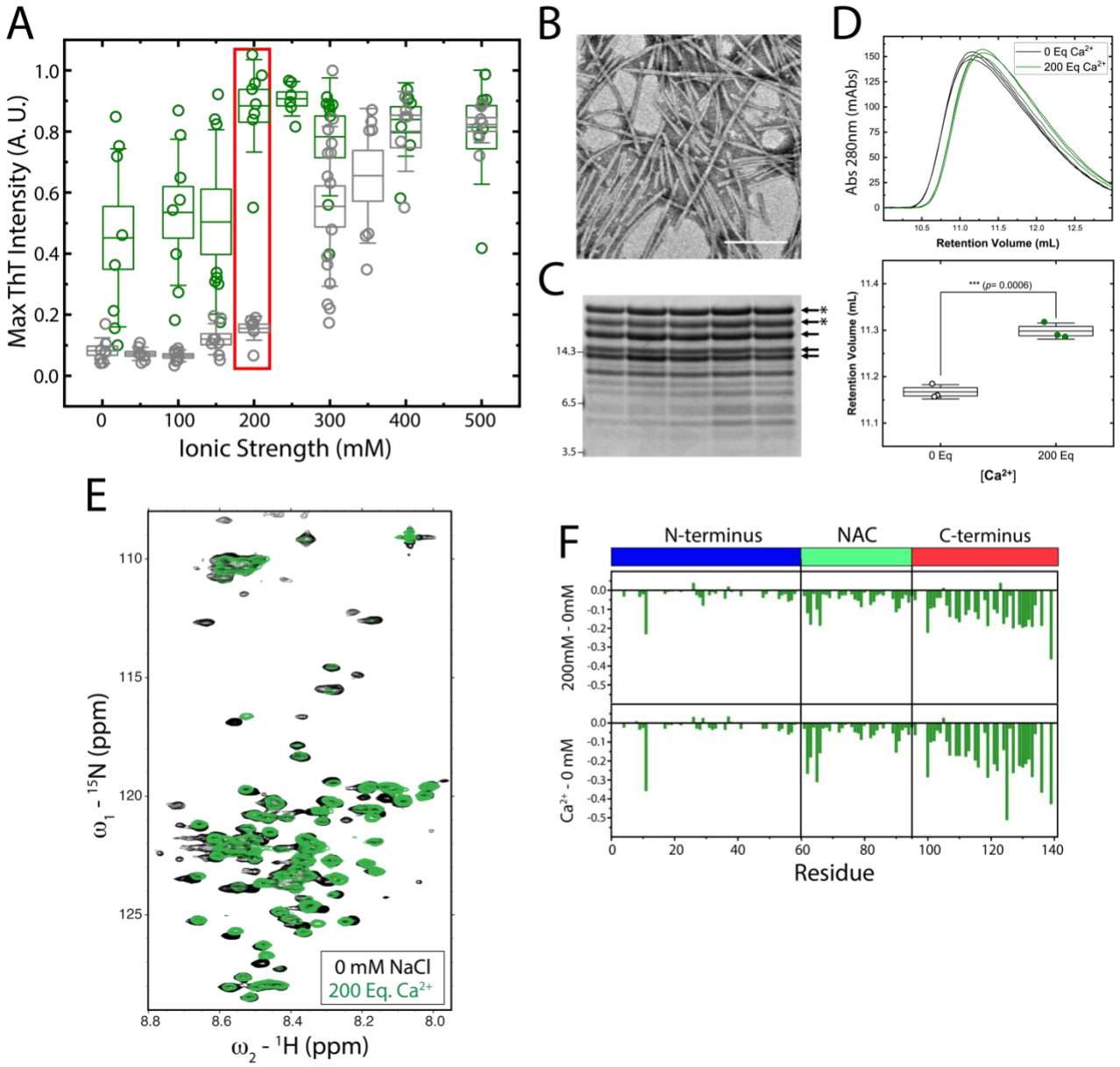

Figure 3. Ca^{2+} enhances the formation of αSyn rod-like fibrils through the compaction of monomers. (A) Maximal ThT intensity values of fibrils created under the indicated ionic strength in the presence (green) or absence (gray) of 200 Eq. Ca^{2+}. (The values of maximal ThT in the absence of Ca^{2+} are the same as those shown in **Fig. 1.B**. They were inserted here for comparative purposes). Boxes represent standard error of the mean values; whiskers represent standard deviation. **(B)** TEM visualization of αSyn fibrils created at an ionic strength of 200 mM in the presence of 200 Eq. Ca^{2+} (Bar scale: 200 nm). **(C)** PKR assay of representative fibrils obtained in the presence of 200 Eq. Ca^{2+} at an ionic strength of 200 mM. Arrows indicate five selected bands subjected to intensity analysis. Bands marked with (*) denote the most relevant differences. Molecular weight markers (kDa) are shown on the left of each panel. **(D)** Representative chromatograms of solutions of monomeric αSyn in the presence or absence of 200 Eq. Ca^{2+}, at an ionic strength of 200 mM, resolved by Size Exclusion Chromatography (top). Retention volume values of αSyn monomers analyzed by SEC in the presence or absence of 200 Eq. Ca^{2+} at an ionic strength of 200 mM (bottom). **(E)** ^{1}H-^{15}N HSQC spectra of αSyn supplemented with 200 Eq Ca^{2+} at an ionic strength of 200 mM (green) compared with αSyn in the absence of Ca^{2+} at an ionic strength of 0 mM (black). (Gray bars represent signals that disappeared in the condition tested but that are present in the reference spectrum) Statistical analyses performed by Student's t-test (B, *** $p < 0.001$).

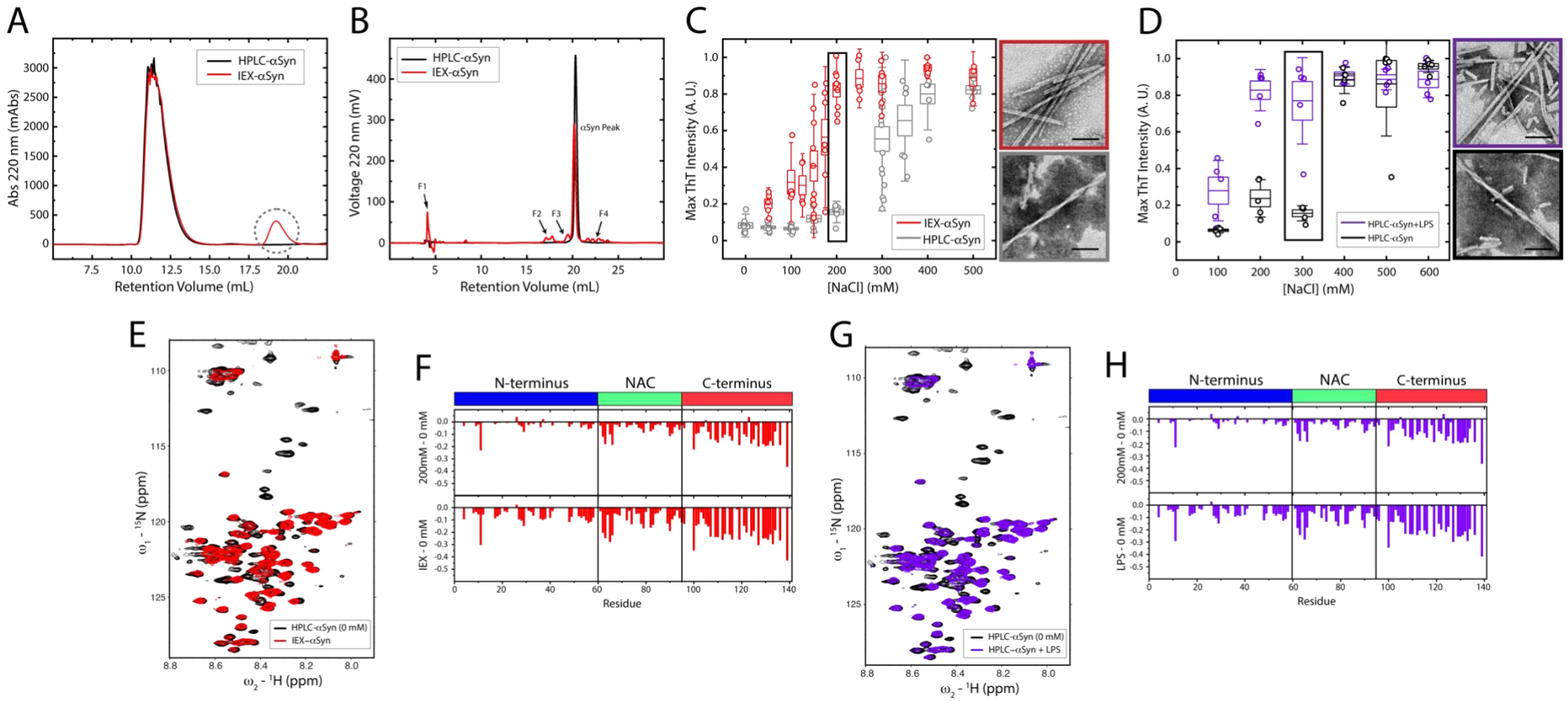
A
HPLC-αSyn
IEX-αSyn
Abs 220 nm (mAbs)
Retention Volume (mL)
B
HPLC-αSyn
IEX-αSyn
Voltage 220 nm (mV)
αSyn Peak
F1
F2
F3
F4
Retention Volume (mL)
C
Max ThT Intensity (A. U.)
IEX-αSyn
HPLC-αSyn
[NaCl] (mM)
D
Max ThT Intensity (A. U.)
HPLC-αSyn+LPS
HPLC-αSyn
[NaCl] (mM)
E
HPLC-αSyn (0 mM)
IEX–αSyn
F
N-terminus
NAC
C-terminus
200mM - 0 mM
IEX - 0 mM
Residue
G
HPLC-αSyn (0 mM)
HPLC–αSyn + LPS
H
N-terminus
NAC
C-terminus
200mM - 0 mM
LPS - 0 mM
Residue

819

Figure 4. Bacterial components present in the purification of recombinant proteins affect the conformational state of the monomeric αSyn. IEX-αSyn and HPLC-αSyn were resolved by analytical size exclusion chromatography **(A)** and analytical reverse phase chromatography **(B)**. **(C)** Left: Maximal ThT intensity values of fibrils created using IEX-αSyn (red) and HPLC-αSyn (gray, taken from **Fig. 1.D** for comparison). Boxes represent standard error of the mean values; whiskers represent standard deviation. Right: TEM visualization of representative fibrils obtained at 200 mM NaCl using IEX-αSyn (upper) and HPLC-αSyn (lower). (Bar scale: 200 nm) **(D)** Left: Maximal ThT intensity values of fibrils created using HPLC-αSyn in the presence (purple) or absence (black) of LPS. Boxes represent standard error of the mean values; whiskers represent standard deviation. Right: TEM visualization of representative fibrils obtained at 300 mM NaCl using HPLC-αSyn in the presence (upper) or absence (lower) of LPS. (Bar scale: 200 nm) **(E)** ^{1}H-^{15}N HSQC spectra of IEX-αSyn at an ionic strength of 200 mM (scarlet) compared with HPLC-αSyn at an ionic strength of 0 mM (black, same as shown in Fig. 3.E). **(F)** Analysis of intensity difference of the N-H nuclei between the spectrum of HPLC-αSyn obtained at 200 mM NaCl versus the spectrum obtained at 0 mM NaCl (upper, same as shown in Fig. 3.F); and the spectrum of IEX-αSyn at an ionic strength of 200 mM versus the spectrum obtained at 0 mM NaCl (lower). (Gray bars represent signals that disappeared in the condition tested but that are present in the reference spectrum) **(G)** ^{1}H-^{15}N HSQC spectra of HPLC-αSyn treated with LPS at an ionic strength of 200 mM (violet) compared with HPLC-αSyn at an ionic strength of 0 mM (black, same as shown in Fig. 3.E). **(H)** Analysis of intensity difference of the N-H nuclei between the spectrum of HPLC-αSyn obtained at 200 mM NaCl versus the spectrum obtained at 0 mM NaCl (upper, same as shown in Fig. 3.F); and the spectrum of HPLC-αSyn plus LPS at an ionic strength of 200 mM versus the spectrum obtained at 0 mM NaCl (lower). (Gray bars represent signals that disappeared in the condition tested but that are present in the reference spectrum).

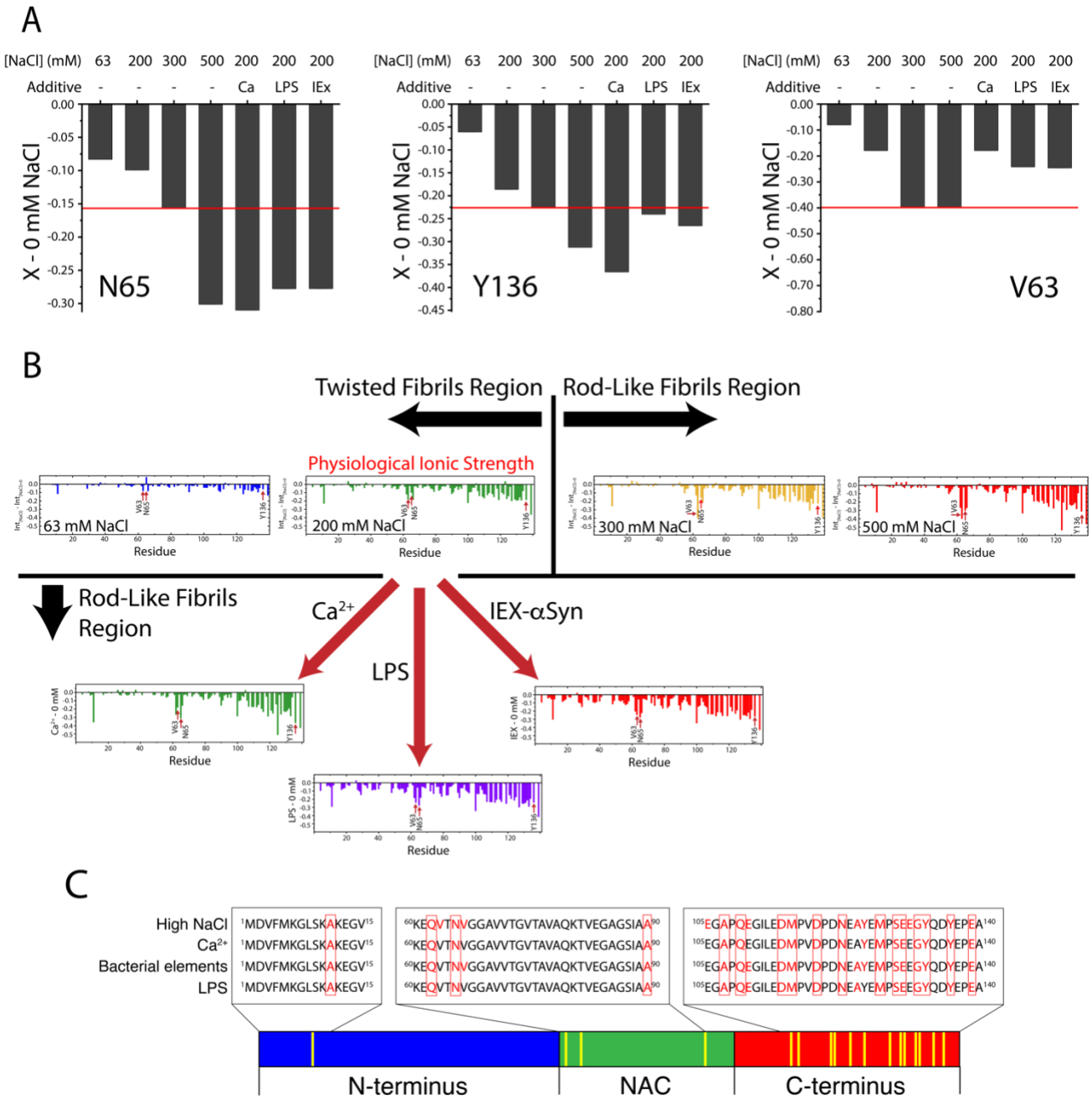

Figure 5. Global analysis of ^{1}H-^{15}N HSQC experiments results. (A) Individual ^{1}H-^{15}N HSQC αSyn peak intensity variation of representative residues under all the conditions tested in this study. The red line represents a threshold established by the peak intensity of the spectrum obtained at 300 mM NaCl. **(B)** Schematic representation of the effect of Ca^{2+}, LPS and bacterial endotoxins on the NMR peak intensity difference and the conformational state of αSyn. **(C)** Alignment of the residues affected by the compaction of αSyn under the conditions indicated in the schematic diagram of panels A and B.

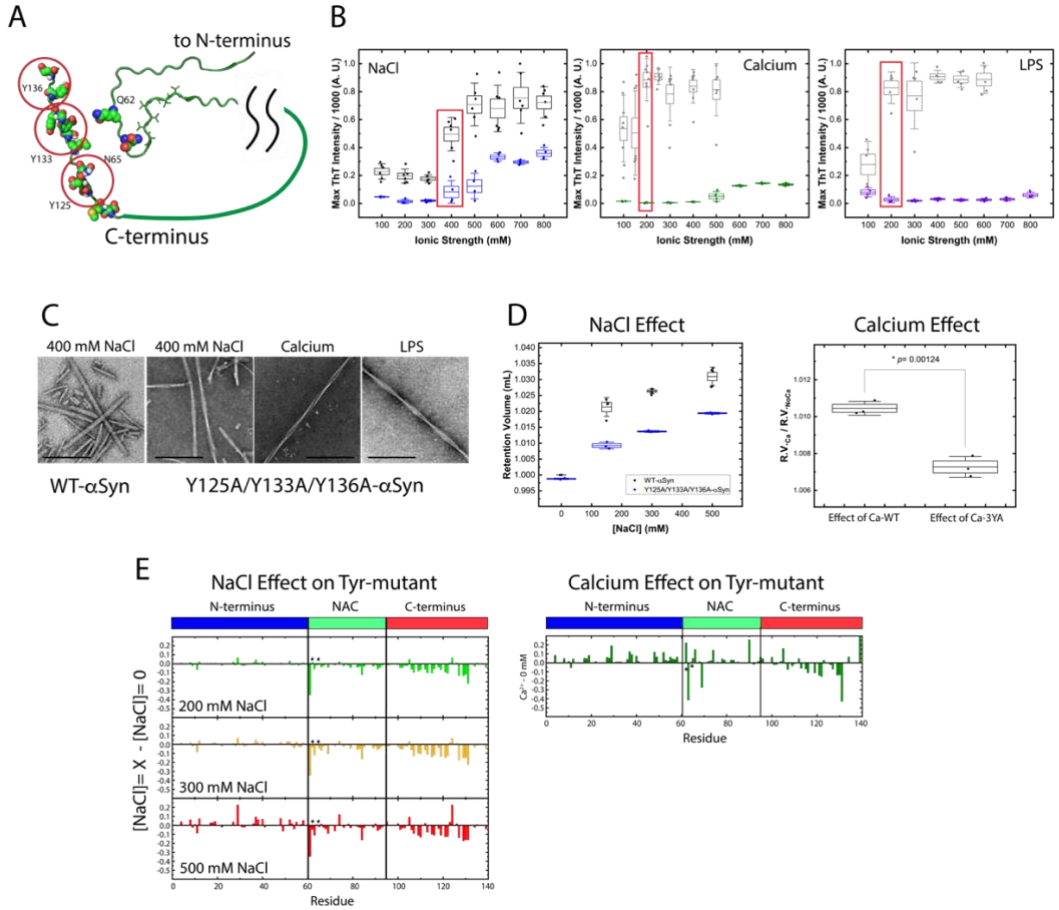

Figure 6. The interaction between the NAC region and the C-terminal domain is intramolecular. (A). Schematic representation of the compact αSyn monomer in which, according to our NMR data, there is an interaction between the residues Q62 and N65 with the C-terminal domain. The red circles indicate the residues that have been modified into Alanine: Tyr125, Tyr133 and Tyr136. **(B)** Maximal ThT intensity values of fibrils created using WT-αSyn (black and gray [gray data obtained for comparison from Fig. 2.A and 4.D. for middle and right panels, respectively]) and the triple mutant Y125A/Y133A/Y135A-αSyn in the presence of various concentrations of NaCl (left, blue), 200 Eq Ca^{2+} (middle, green), and 50 µg/mL LPS (right, purple), under the indicated ionic strength. The red squares highlight the shifting of the inflection point suffered in the triple Tyrosine mutants compared with the WT-αSyn. Boxes represent standard error of the mean values, whiskers represent standard deviation. **(C)** TEM visualization of representative fibrils obtained of WT-αSyn with NaCl (400 mM NaCl), and Y125A/Y133A/Y136A-αSyn with NaCl (400 mM NaCl), 200 Eq. Ca^{2+} (200 mM IS), and 50 µg/mL LPS (200 mM IS). (Bar scale: 200 nm). **(D)** Left: Normalized retention volume values of solutions of WT-αSyn (black) and Y125A/Y133A/Y136A-αSyn (blue) resolved by SEC. Right: Effect of 200 Eq Ca^{2+} on the conformational state of WT-αSyn and the triple mutant Y125A/Y133A/Y136A-αSyn (3YA) evaluated by SEC through he parameter $R.V._{Ca}$ / $R.V._{NoCa}$. Boxes represent standard error of the mean values; whiskers represent standard deviation. **(E)** Left: Peak intensity difference analysis of the spectra of Y125A/Y133A/Y136A -αSyn of the amide N-H nuclei recorded at 200 mM, 300 mM, and 500 mM NaCl, employing the spectrum obtained at 0 mM NaCl as a reference. The asterisks represent the peak intensity variations of Q62 and N65. Right: Analysis of intensity difference of the N-H nuclei between the spectrum of Y125A/Y133A/Y136A-αSyn obtained at 200 mM NaCl in the absence of Ca^{2+} versus the spectrum obtained at 0 mM NaCl (upper); and the spectrum in the presence of 200 Eq. Ca^{2+} at an ionic strength of 200 mM versus the spectrum obtained at 0 mM NaCl (lower).–(Gray bars represent signals that disappeared in the condition tested but that are present in the reference spectrum). The asterisks represent the peak intensity variations of Q62 and N65. Statistical analyses performed by Student's t-test (D, * $p < 0.05$).

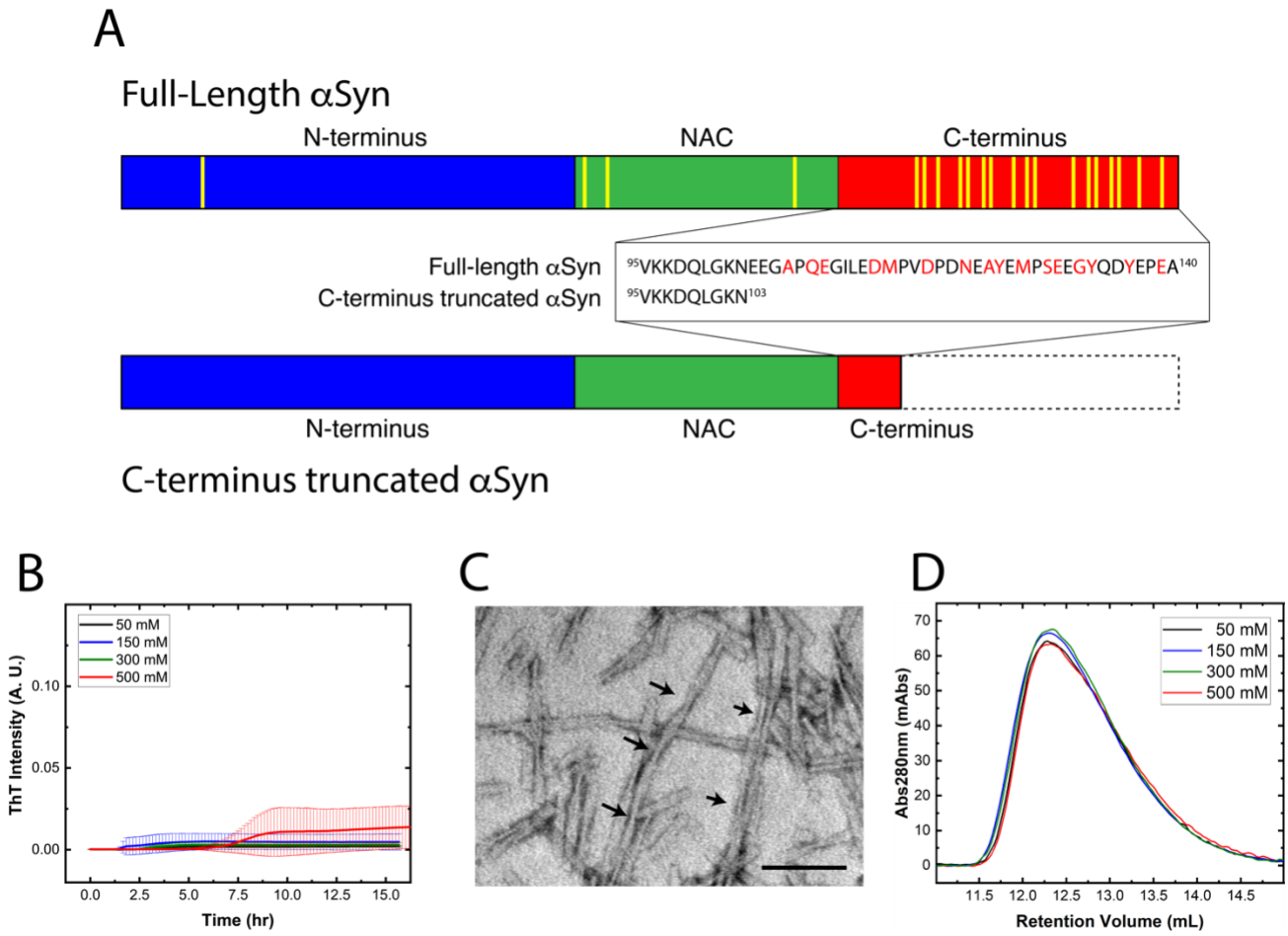

Figure 7. N103t-C terminus truncated αSyn does not adopt the compact conformation. (A) Schematic representation of the truncated form N103t, in which the region detected to be relevant for the compaction of the monomers (residues highlighted in red, according to the algorithm shown in the **Fig. S9**) has been removed. **(B)** ThT-monitored fibril formation of C-terminus truncated N103t αSyn at 50, 150, 300, and 500 mM NaCl. The graph represents the average of at least 6 replicates at each concentration of salt indicated. The error bars indicate the standard deviation. **(C)** TEM visualization of N103t αSyn fibrils generated at 500 mM NaCl. The arrows represent twists in the fibrils. (Bar scale: 100 nm). **(D)** Representative chromatograms of solutions of N103t αSyn at different concentrations of NaCl resolved by Size Exclusion Chromatography.